



A Journal of the Gesellschaft Deutscher Chemiker

Angewandte Chemie

GDCh

International Edition

www.angewandte.org

Accepted Article

Title: Surface engineering of g-C₃N₄ by stacked oxygen vacancies-rich BiOBr sheets for boosting photocatalytic performance

Authors: Dongni Liu, Dongyun Chen, Najun Li, Qingfeng Xu, Hua Li, Jinghui He, and Jian-Mei Lu

This manuscript has been accepted after peer review and appears as an Accepted Article online prior to editing, proofing, and formal publication of the final Version of Record (VoR). This work is currently citable by using the Digital Object Identifier (DOI) given below. The VoR will be published online in Early View as soon as possible and may be different to this Accepted Article as a result of editing. Readers should obtain the VoR from the journal website shown below when it is published to ensure accuracy of information. The authors are responsible for the content of this Accepted Article.

To be cited as: *Angew. Chem. Int. Ed.* 10.1002/anie.201914949
Angew. Chem. 10.1002/ange.201914949

Link to VoR: <http://dx.doi.org/10.1002/anie.201914949>
<http://dx.doi.org/10.1002/ange.201914949>

RESEARCH ARTICLE

Surface engineering of g-C₃N₄ by stacked oxygen vacancies-rich BiOBr sheets for boosting photocatalytic performance

Dongni Liu, Dongyun Chen, Najun Li, Qingfeng Xu, Hua Li, Jinghui He, and Jianmei Lu*

Abstract: BiOBr containing surface oxygen vacancies (OVs) was prepared by a simple solvothermal method and combined with graphitic carbon nitride (g-C₃N₄) to construct a heterojunction for photocatalytic oxidation of nitric oxide (NO) and reduction of carbon dioxide (CO₂). The formation of the heterojunction enhanced the transfer and separation efficiency of photogenerated carriers. Furthermore, the surface OVs sufficiently exposed catalytically active sites, and enabled capture of photoexcited electrons at the surface of the catalyst. Internal recombination of photogenerated charges was also limited, which contributed to generation of more active oxygen for NO oxidation. Heterojunction and OVs worked together to form a spatially conductive network framework, which achieved 63% NO removal, 96% selectivity for carbonaceous products (i.e., CO and CH₄). The stability of the catalyst was confirmed by cycling experiments and X-ray diffraction and transmission electron microscopy after NO removal.

Introduction

Environmental pollution is a global concern. Nitric oxide (NO) is the main cause of acid rain and photochemical smog and a major component of automobile exhaust fumes. The reduction of NO by selective catalytic reduction (SCR) requires a high temperature environment and a reducing agent NH₃,^[1] which is complex and time consuming. At low NO concentrations, photocatalytic oxidation is a green and environmentally effective removal measure. Semiconductor catalysts, such as graphitic carbon nitride (g-C₃N₄),^[2] Bi-based materials^[3] and metal oxides,^[4] are widely used in the field of photocatalysis owing to their appropriate band gap. However, photoexcited charges inside the semiconductor easily recombine, resulting in low catalytic activity. A heterostructure alleviates the above problems to a certain extent by enhancing the separation efficiency of photogenerated carriers, suppressing the internal integration of a large number of electron-hole pairs in the pure semiconductor and broadening the visible light response range of the single catalyst.

In recent years, the advantages of oxygen vacancies (OVs) in photocatalytic redox have been highlighted, owing to their ability to capture electrons, decrease band gaps, and promote surface adsorption of substrate molecules. The use of OVs in photocatalysis is common. Shang et al. designed and synthesized blue TiO₂ with oxygen vacancies for NO photooxidation;^[5] Jin et

al. used an OV-engineered Bi₂₄O₃₁Cl₁₀ sample for CO₂ photoreduction;^[6] Li et al. fabricated SrTiO₃ nanofibers with OVs, which were applied for H₂ production.^[7] High temperature polyol pyrolysis and inert gas calcination produced a large amount of bulk OVs, which caused internal recombination of the excited carriers and weakened degradation efficiency.^[8] In the case of bulk OVs, the sheet morphology reduced the charge migration distance and improved the transfer ability of electron-hole pairs. The water-ethylene glycol mixed solvothermal method also increased the concentration of surface OVs and the content of reduced bulk OVs. In the synthesis of OV-containing BiOX (X = Cl, Br, I), the introduction of water promoted solvation of Bi³⁺ in the raw material bismuth nitrate pentahydrate and nucleation and growth of BiOX was achieved at room temperature.^[9] Subsequent high temperature solvothermal caused the electrons of ethylene glycol (EG) to reduce Bi, break Bi-O bonds, and ultimately form surface OVs. Similarly, the formation of a loose flower-like BiOBr in this article is attributed to addition of water, which reduced the viscosity of the system and avoided the formation of particulate spheres. As a result, the emergence of surface OVs further inhibited the charge recombination rate of the flower-like BiOBr consist of stacked nanosheets. The g-C₃N₄ has a wide band gap and two-dimensional layered characteristics, which contribute to excellent photocatalytic performance.^[2a] The large sheet structure contributes to a high contact area between the supported catalyst and the substrate catalyst and improves the separation efficiency of photogenerated carriers.

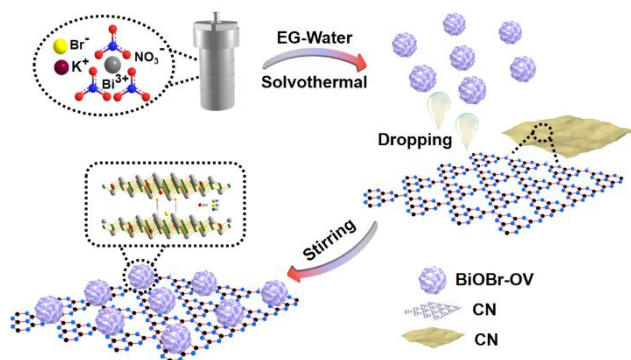
On the basis of the above analysis, we designed and synthesized a BiOBr-g-C₃N₄ heterojunction system rich in surface OVs (denoted as CN-BiOBr-OV) and used it for photocatalytic removal of NO (**Scheme 1**). The OVs contributed to conversion of CO₂ into value-added carbonaceous products (e.g., CH₄, HCHO, and CH₃OH).^[6] This conversion alleviates environmental damage and energy consumption caused by fossil fuel combustion. In the case of a composite heterojunction, the three-dimensional-two-dimensional (3D-2D) combination constituted a spatially conductive network framework, resulting in enhanced separation efficiency of electron-hole pairs. In addition, the presence of surface OVs caused electrons to be trapped at the surface of the BiOBr, which reduced the internal carrier recombination and increased the amount of active oxygen free radicals, which facilitated NO catalytic performance. The loose flower-like structure of BiOBr facilitated circulation of the exhaust. Surface OVs provided catalytically active sites for adsorption of substrate molecules and completion of the reaction. This 3D-2D heterojunction with surface OVs synergistically promotes photocatalysis and may have broad application potential in environmental purification and other fields.

D.N. Liu, Prof. D.Y. Chen, Prof. N.J. Li, Prof. Q.F. Xu, Prof. H. Li, Prof. J.H. He, and Prof. J.M. Lu,
College of Chemistry, Chemical Engineering and Materials Science
Collaborative Innovation Center of Suzhou Nano Science and
Technology
Soochow University
Suzhou 215123 (P. R. China)

lujm@suda.edu.cn

Supporting information for this article is given via a link at the end of the document.

RESEARCH ARTICLE



Scheme 1. Schematic illustration of the synthetic procedure of CN-BiOBr-OV.

Results and Discussion

The crystalline phases of the synthesized catalysts were determined by X-ray diffraction (XRD) measurements. **Figures 1a** and **S1a** show diffraction patterns of CN, BiOBr, BiOBr-OV, and their composites. Two typical peaks of CN (JCPDS#87-1526) were located at 12.6° 2θ and 27.7° 2θ , respectively. The (002) peak with greater intensity derives from interlayer stacking of conjugated aromatic ring segments, whereas the weaker (100) peak is formed by an in-plane structural repeating motif in the N-linked heterocyclic system.^[10] The diffraction peaks of BiOBr-OV are indexed to the P4/nmm tetragonal phase BiOBr (JCPDS#09-0393).^[9] Furthermore, the (001) and (102) planes of BiOBr-OV markedly widened, indicating that the nanosheets of the nanoflowers were thin. After coupling of BiOBr and BiOBr-OV with CN, the (002) plane of the CN and the corresponding diffraction peaks of BiOBr were observed in the composites, which confirmed their stable bonding.

The chemical states and structural environments of elements in CN-BiOBr-OV hybrid were evaluated by XPS. The binding energies were calibrated against the C 1s peak at 284.8 eV. **Figures 1c-f** and **S2** show the full and high resolution spectra of C 1s, N 1s, O 1s, Br 3d, and Bi 4f regions for CN-BiOBr-OV sample. The signal peak of C 1s was fitted to three regions at 284.8, 286.2, and 288.4 eV, which we attribute to bonding of C-C, C-N, and N-C=N, respectively.^[11] The spectrum of N 1s was composed of four nitrogen species in the CN framework, corresponding to C-N=C at 398.7 eV, N(N-(C)₃) at 399.4 eV, N-H at 400.7 eV, and π excitations at 404.4 eV. The remaining peaks in composite have hardly shifted except for the sharp decrease of π excitations peaks that almost disappear. It shows that BiOBr-OV is bonded to π electrons in C-N heterocycles of CN.^[12] In addition, the weakening of the peak intensity of C-N heterocycles of CN-BiOBr-OV in FT-IR spectra also complement the above-mentioned interaction (**Figure S1b**). For O1s, The first peak is assigned to Bi-O in the crystal structure of $[\text{Bi}_2\text{O}_2]^{2+}$; the second peak (530.8 eV) is the signal of oxygen species in the PVP surfactant; the third is the chemical binding energy state of oxygen atoms near OVs in the BiOBr-OV catalyst; the last is the surface

hydroxyl groups. XPS analysis indicates the coexistence of two components and interactions between them in the CN-BiOBr-OV. The electron spin resonance (ESR) results in **Figure 1b** also show BiOBr-OV and its composite with CN with a obvious OV signal ($g = 2.004$), which is consistent with the XPS fitting. No signals from OVs appeared in BiOBr control sample.

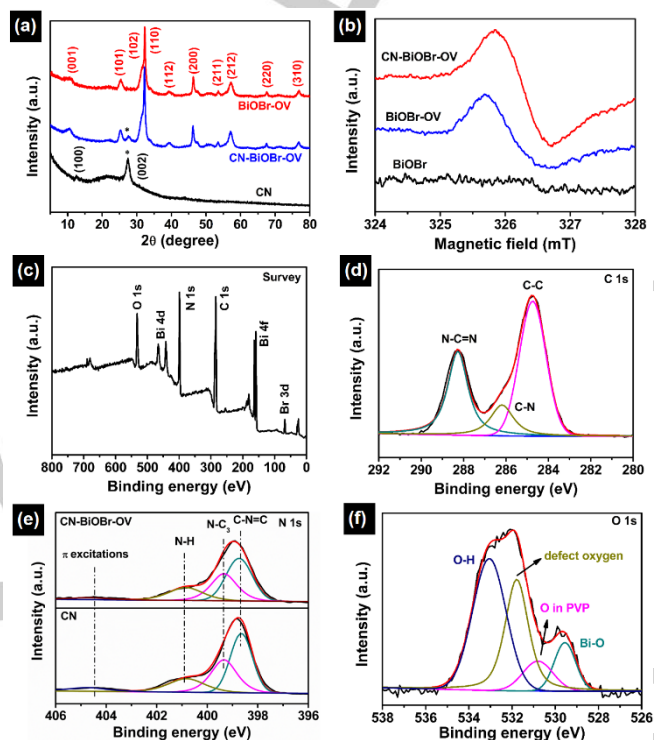


Figure 1. (a) XRD patterns of CN, BiOBr-OV and CN-BiOBr-OV samples, (b) ESR spectra (at 298 K). XPS spectra of (c) survey scan, and high-resolution of (d) C 1s, (e) N 1s and (f) O 1s.

Figures 2 and **3** show the microstructures of CN, BiOBr, BiOBr-OV, CN-BiOBr and CN-BiOBr-OV observed in scanning electron microscope (SEM), transmission electron microscope (TEM), and high resolution (HR)-TEM imaging. Layered CN has a pleated structure and several micrometers in size (**Figure 2a**), which also appear in the TEM image (**Figure 3a**). **Figure 3a** also shows the CN as ultrathin irregular nanosheets. Nanoflower-like BiOBr crystals with OVs were synthesized by a simple solvothermal method (**Figures 2b** and **3c**). We confirmed that the nanoflowers were formed by self-assembly of stacked 400 nm nanosheets (**Figure 2b**). When the nanoflowers were loaded on the CN, their morphology and particle size were retained and no agglomeration or scattering occurred (**Figures 2c, d** and **3d**). The segmented interface shown in the (HR)-TEM image of the CN and BiOBr-OV indicates strong interaction between the heterojunction with OVs (**Figure 3e**), which facilitated charge separation in the photocatalytic process. The BiOBr-OV had clear crystal lattice fringes, which also indicated good crystallinity. The lattice spacings of $d = 0.280$ and $d = 0.352$ nm correspond to the (102) and (101) crystal planes of the tetragonal phase BiOBr, respectively (**Figures 3e** and **f**). To emphasize the advantages of

RESEARCH ARTICLE

OVs, we also synthesized BiOBr nanosheets without OVs and their hybrids with CN for comparison (Figures 2e, f and 3b). Figure 3g is an elemental-mapping image of the CN-BiOBr-OV heterojunction, which indicates that five elements C, N, O, Br, and Bi coexisted in both components, consistent with the SEM-mapping results (Figure S3).

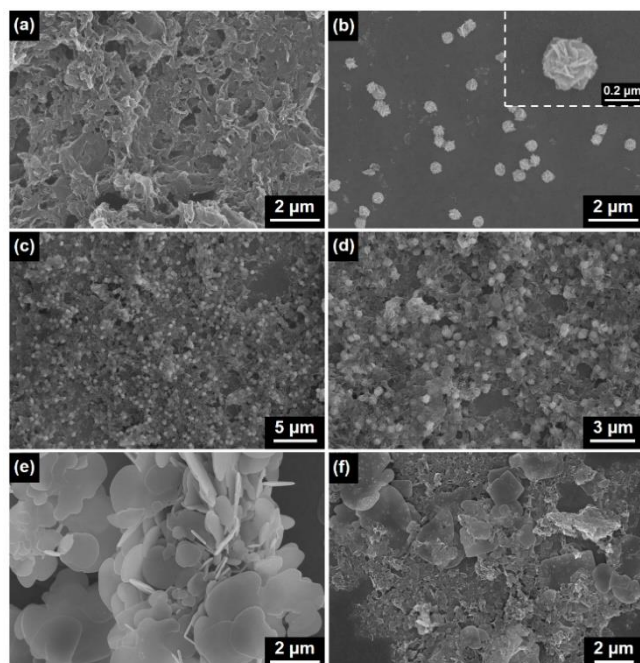


Figure 2. SEM images of (a) CN, (b) BiOBr-OV, (c, d) CN-BiOBr-OV at different magnification levels, (e) BiOBr, and (f) CN-BiOBr.

The UV-Vis diffuse reflectance spectroscopy results are shown in Figure 4a. The CN formed by polycondensation of urea had a basic absorption edge of approximately 430 nm. After coupling with BiOBr crystal plane, the absorption features of the prepared CN-BiOBr and CN-BiOBr-OV samples were located between the two components. Conversely, the BiOBr-OV and CN-BiOBr-OV curves had long tails with distinct slopes on the right side and tangents ($Y = 0$) extending to the horizontal axis at 700 and 750 nm, which indicates that the defect levels might influence their light harvesting ability. Besides, the band gaps (E_g) of CN, BiOBr and BiOBr-OV were calculated from the fitting formula $dh\nu = A(h\nu - E_g)^{n/2}$ (indirect transition $n = 4$) to be 2.79, 2.60, and 2.53 eV, respectively (Figure S4a). The interfacial band structure and visible light response are expected to be favorable factors for photocatalysis.

On the basis of the above studies, we speculate that the performance of the OVs-rich CN-BiOBr heterojunction was most prominent. Therefore, we used PL to examine the separation and transfer ability of the photoexcited electron-hole pairs of CN-BiOBr-OV. As shown in Figure 4b, the fluorescence intensity of the composite samples was lower than that of their substrate catalyst CN, mainly because of the restructuring of photogenerated carriers inhibited by loading of BiOBr. For CN-

BiOBr-OV, the presence of OVs increased the ability to capture electrons, thereby prolonging the lifetime of charges and enhancing the use of electrons and holes in redox process.

Electrochemical impedance spectroscopy (EIS) and photocurrent density versus time response spectra show the relative photoinduced charge transfer ability. Clearly, CN-BiOBr-OV had the strongest photocurrent density, which corresponded to carrier separation with superior efficiency. The data in Figure 4c indicated that the photocurrent densities of the OVs-rich composite catalyst were 6.2, 2.4, and 1.3 times the response values of CN, BiOBr-OV, and CN-BiOBr, respectively. Notably, the variations of the current density (ΔI_1 and ΔI_2) are due to the enhancement of the separation efficiency of electron-hole pairs stems from the construction of heterojunctions with OVs, which promotes an increase in electron density.^[13] The slope of the Nyquist curve, as shown in the EIS spectra also gives the results (Figure 4d), which is consistent with the photocurrent transient responses and PL results. On this basis, the combined effects of the OVs and heterojunction have an important influence on the photoelectric properties.

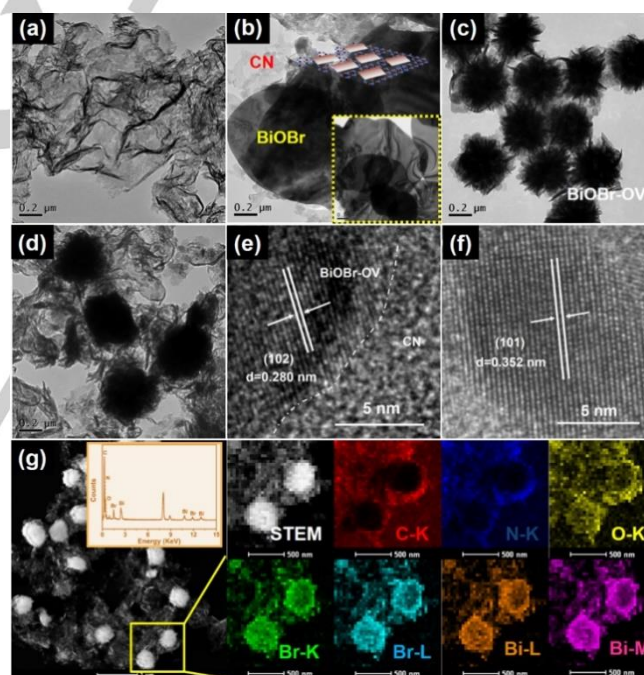


Figure 3. TEM images of (a) pure CN, (b) CN-BiOBr, and BiOBr marked in the lower right corner, (c) bare BiOBr-OV, (d) CN-BiOBr-OV catalyst, (e, f) HR-TEM images of CN-BiOBr-OV heterojunction with the lattice spacings, and (g) elemental maps of C, N, O, Br, and Bi in the CN-BiOBr-OV photocatalyst.

The photocatalytic oxidation gently removed low concentrations (600 ppb) of NO at room temperature, which is of practical importance for indoor air purification. Under typical operation, the investigated catalysts were placed in a reaction chamber for 30 min to achieve an adsorption-desorption balance of air and NO to be treated. The results of the photocatalytic tests after illumination are shown in Figures 5a and S5. The degradation efficiency of

RESEARCH ARTICLE

the BiOBr sample without OV's after equilibrium reached only 11%. The tail later turned up owing to subsequent desorption of the fluffy powder state. The BiOBr-OV nanoflowers after modification with OV's achieved 40% removal rate, which was almost the same as the CN-BiOBr heterojunction. Unexpectedly, the degradation efficiency of CN-BiOBr-OV was as high as 63%, i.e., 1.8, 1.6, 1.6 and 1.5 times as high as those of CN, BiOBr-OV, CN-BiOBr, and the physical mixture of CN and BiOBr-OV, respectively. Hence, the synergistic effects of the OV's and heterojunction greatly enhanced the separation and transfer ability of photogenerated carriers. This study found that the degradation was superior to most other single catalysts with OV's (Table S1). Moreover, a notably low amount of NO₂ was produced by CN-BiOBr-OV (Figure S6), which contributed to a large amount of NO conversion to NO₃⁻. The recycling performance of the catalyst is critical for its cost performance and practical applications. We performed five cycles of testing on CN-BiOBr-OV, and the degradation effect was only slightly weakened (Figure 5b). XRD and TEM characterization of the degraded samples remained intact (Figure S7), indicating the excellent stability.

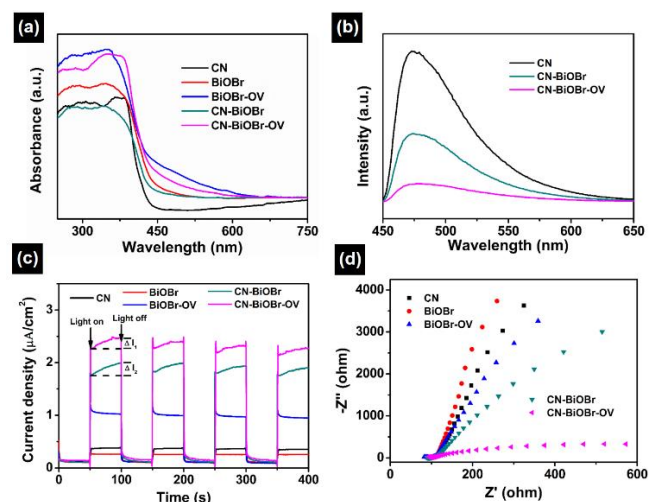


Figure 4. (a) UV-Vis spectra, (b) PL spectra (excitation wavelength at 395 nm), (c) Photocurrent density response, and (d) EIS spectra of as-synthesized samples under visible light.

Considering the excellent activity of OV's in capturing photogenerated electrons, photocatalytic CO₂ conversion has also been used to study the properties of different catalysts. As shown in Figure 5e, the yield rates of CO and CH₄ on pure CN were 29.5 and 13.1 μmol h⁻¹ g⁻¹, respectively. For BiOBr-OV, the CO production was similar to that of BiOBr alone except that BiOBr-OV produced 17.3 μmol h⁻¹ g⁻¹ of CH₄. Based on facts, the production of CO requires 2e⁻/2H⁺, while the production of CH₄ needs 8e⁻/8H⁺.^[14] BiOBr-OV is rich in OV's, which can capture more photo-generated electrons to promote the carrier separation, and the electron density is increased for CH₄ production. After BiOBr-OV and CN formed a heterojunction, the evolution rates of CO and CH₄ corresponded to 61.8 and 27.1 μmol h⁻¹ g⁻¹, respectively, which were greater than that of the heterojunction

CN-BiOBr without OV's. The carbonaceous product (i.e., CO and CH₄) selectivity of CN-BiOBr-OV was countered by H₂, reaching 96%. In a control experiment (Figure S8), in the absence of the catalyst and light, a negligible amount of product formed, indicating the need to illuminate the prepared sample. In addition, the use of Ar gas rather than CO₂ produced only a small amount of H₂, indicating that the CO and CH₄ were produced by reduction of CO₂ carried in the water vapor. Finally, we conducted the cycling experiments to test and verify the stability of the catalyst and found that the degradation efficiency was consistent over five cycles (Figure 5f).

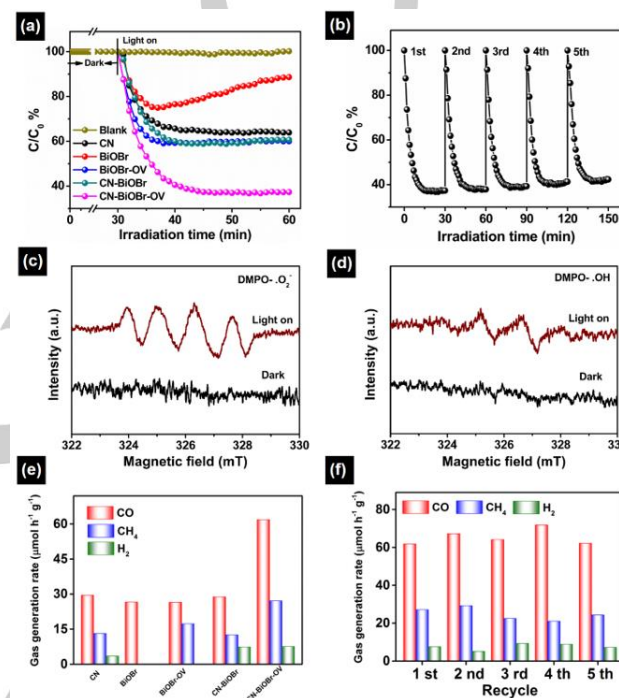


Figure 5. (a) NO removal experiment under visible light irradiation, (b) photocatalytic activities of CN-BiOBr-OV after five consecutive cycles, and ESR profiles of (c) DMPO-•O₂⁻ and (d) DMPO-•OH for CN-BiOBr-OV heterojunction, (e) Photocatalytic CO₂ conversion over different catalysts and (f) cyclic stability testing on the CN-BiOBr-OV composite.

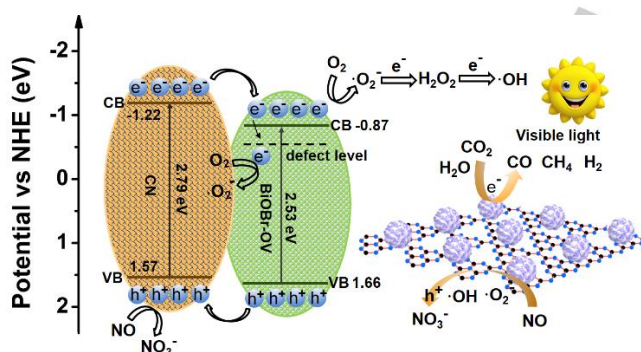
To explore the mechanism of photocatalysis, we used ESR and fluorescence to detect active species generated under illumination conditions. As shown in Figure 5c, four similar characteristic peaks of superoxide radicals (•O₂⁻) produced by CN-BiOBr-OV were present after turning on the light source. The peak intensity in Figure 5d exhibited a typical 1:2:2:1 characteristic corresponding to the signal of the hydroxyl group (•OH). Compared with the weak peaks under dark conditions, the peak value of CN-BiOBr-OV after photoexcitation was markedly boosted, indicating an increase in the number of free radicals. Capture experiments have also verified that •O₂⁻ and •OH play an important role with electrons and holes (Figure S9).

On the basis of the above measurements, we examined the mechanism of the photocatalytic degradation process in depth. First, CN and BiOBr-OV generated photogenerated electron-hole

RESEARCH ARTICLE

pairs inside the semiconductor after light irradiation. Combining the valance band-XPS pattern and the band gap fitting in **Figure S4**, the conduction band (CB) levels were assigned to -1.22 eV for CN and -0.87 eV for BiOBr-OV. Because the CB of BiOBr-OV is lower than that of CN, the electrons (e^-) were transferred from the CB of CN to BiOBr-OV. The liquid fluorescence results showed that the light-induced process produced H_2O_2 and $\cdot OH$ (**Figure S10**),^[15] and $\cdot OH$ also played an important role in degradation of NO. Holes (h^+) were transferred from the valance band of BiOBr-OV to CN, and h^+ carried water in the air to oxidize NO to NO_3^- . In addition, BiOBr captured e^- transferred from the CB of CN and its own CB to surface OVs. Subsequently, the adsorbed oxygen at OVs reacted with the e^- to generate more active $\cdot O_2^-$ for NO removal. During the photocatalytic process, the surface OVs worked with the heterojunction to promote photocatalytic oxidation, which greatly increased the removal efficiency of exhaust gas NO. The radical evolution process is drawn in the equations (**S13**) and **Scheme 2**.

The mechanism of photocatalytic CO_2 reduction is also described in **Scheme 2**. The h^+ were quenched by TEOA to produce $TEOA^+$. The e^- at the CB of BiOBr-OV and e^- captured by OVs reduced CO_2 molecules on the catalyst surface to CO and CH_4 carbonaceous materials with redox potentials of $CO/CO_2 = -0.53$ eV and $CO/CH_4 = -0.24$ eV.^[14, 16] These values are more positive than the CB potential of BiOBr-OV and the evolution of H_2 derived from H_2O molecules.



Scheme 2. Schematic illustration of the photocatalytic mechanism of NO removal and CO_2 conversion.

Conclusion

In this paper, BiOBr with surface OVs was synthesized by a solvothermal method and combined with CN to form a heterojunction for removal of low concentrations (600 ppb) of NO and photoreduction of CO_2 at room temperature under visible light irradiation. The formation of a heterojunction promoted separation of electron-hole pairs, which improved the carrier separation efficiency of the single catalysts; surface OVs tended to capture electrons on the surface of BiOBr to reduce internal charge recombination, which in turn produced more reactive oxygen radicals for photocatalytic NO removal. The OVs and

heterojunction synergistically promoted rapid advancement of photodegradation. As a result, CN-BiOBr-OV achieved a catalytic efficiency of 63% on NO degradation and selectivity of 96% of carbonaceous products on CO_2 conversion. The efficiency after five cycles remained relatively unchanged, which also confirmed the stability of the synergistic composite.

Acknowledgements

We gratefully acknowledge the financial support provided by the National Key R&D Program of China (2017YFC0210901, 2017YFC0210906), National Natural Science Foundation of China (51573122, 21722607, 21776190), Natural Science Foundation of the Jiangsu Higher Education Institutions of China (17KJA430014, 17KJA150009), the Science and Technology Program for Social Development of Jiangsu (BE2015637) and the project supported by the Priority Academic Program Development of Jiangsu Higher Education Institutions (PAPD). We gratefully acknowledge Dr. Ying Wang, Jing Ye, Xing Zhu, Muzi Chen and Jun Guo from the Testing and Analysis Center of Soochow University for characterizations. We also gratefully acknowledge Dr. Xingwang Zhu, Prof. Hui Xu from Institute for Energy Research of Jiangsu University.

Keywords: Surface oxygen vacancies • Heterojunction • NO oxidation • CO_2 reduction

- [1] L. Ma, C. Y. Seo, M. Nahata, X. Chen, J. Li, J. W. Schwank, *Appl. Catal. B* **2018**, 232, 246-259.
- [2] a) W. J. Ong, L. L. Tan, Y. H. Ng, S. T. Yong, S. P. Chai, *Chem. Rev.* **2016**, 116, 7159-7329; b) J. Hu, D. Chen, N. Li, Q. Xu, H. Li, J. He, J. Lu, *Small* **2018**, 14, 1800416.
- [3] a) L. Hao, L. Kang, H. Huang, L. Ye, K. Han, S. Yang, H. Yu, M. Batmunkh, Y. Zhang, T. Ma, *Adv. Mater.* **2019**, 31, 1900546; b) M. Li, S. Yu, H. Huang, X. Li, Y. Feng, C. Wang, Y. Wang, T. Ma, L. Guo, Y. Zhang, *Angew. Chem. Int. Ed.* **2019**, 58, 9517-9521.
- [4] S. Xiao, D. Zhang, D. Pan, W. Zhu, P. Liu, Y. Cai, G. Li, H. Li, *Nat. Commun.* **2019**, 10, 1570.
- [5] H. Shang, M. Li, H. Li, S. Huang, C. Mao, Z. Ai, L. Zhang, *Environ. Sci. Technol.* **2019**, 53, 6444-6453.
- [6] X. Jin, C. Lv, X. Zhou, L. Ye, H. Xie, Y. Liu, H. Su, B. Zhang, G. Chen, *ChemSusChem* **2019**, 12, 2740-2747.
- [7] C. Li, S. Yi, D. Chen, Y. Liu, Y. Li, S. Lu, X. Yue, Z. Liu, *J. Mater. Chem. A* **2019**, 7, 17974-17980.
- [8] F. Chen, H. Huang, L. Guo, Y. Zhang, T. Ma, *Angew. Chem. Int. Ed.* **2019**, 58, 10061-10073.
- [9] X. Tong, X. Cao, T. Han, W. Cheong, R. Lin, Z. Chen, D. Wang, C. Chen, Q. Peng, Y. Li, *Nano Res.* **2019**, 12, 1625-1630.
- [10] J. Ran, T. Pan, Y. Wu, C. Chu, P. Cui, P. Zhang, X. Ai, C. F. Fu, Z. Yang, T. Xu, *Angew. Chem. Int. Ed.* **2019**, 58, 16463-16468.
- [11] Q. Liu, C. Zeng, Z. Xie, L. Ai, Y. Liu, Q. Zhou, J. Jiang, H. Sun, S. Wang, *Appl. Catal. B* **2019**, 254, 443-451.
- [12] a) W. Jo, S. Kumar, S. Eslava, S. Tonda, *Appl. Catal. B* **2018**, 239, 586-598; b) B. Krüner, C. Odenwald, A. Quade, G. Kickelbick, V. Presser, *Batteries & Supercaps* **2018**, 1, 135-148.
- [13] a) F. Chen, H. Huang, L. Ye, T. Zhang, Y. Zhang, X. Han, T. Ma, *Adv. Funct. Mater.* **2018**, 28, 1804284; b) H. Huang, S. Tu, C. Zeng, T. Zhang, A. H. Reshak, Y. Zhang, *Angew. Chem. Int. Ed.* **2017**, 56, 11860-11864.
- [14] Z. Sun, N. Talreja, H. Tao, J. Texter, M. Muhler, J. Strunk, J. Chen, *Angew. Chem. Int. Ed.* **2018**, 57, 7610-7627.

RESEARCH ARTICLE

- [15] G. Dong, L. Yang, F. Wang, L. Zang, C. Wang, *ACS Catal.* **2016**, 6, 6511-6519.
- [16] H. Takeda, K. Ohashi, A. Sekine, O. Ishitani, *J. Am. Chem. Soc.* **2016**, 138, 4354-4357.

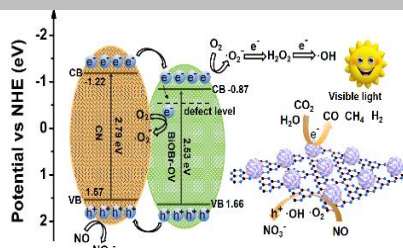
WILEY-VCH

Accepted Manuscript

RESEARCH ARTICLE

RESEARCH ARTICLE

Sheet-stacked oxygen vacancies-rich BiOBr nanoflowers are prepared by a simple solvothermal process and form a heterojunction with graphitic carbon nitride. Oxygen vacancies and heterojunction synergistically promote photocatalysis, achieving a NO degradation effect of 63% and 96% selectivity of carbonaceous products for CO₂ conversion.



Dongni Liu, Dongyun Chen, Najun Li, Qingfeng Xu, Hua Li, Jinghui He, and Jianmei Lu*

Page No. – Page No.

Surface engineering of g-C₃N₄ by stacked oxygen vacancies-rich BiOBr sheets for boosting photocatalytic performance